



Original article

3D printed and circularly polarized 28 GHz patch antenna array for small satellite communications

Jengsu Yoo ¹, Myung Lae Lee ¹, Yong Suk Yang ^{1,*}*Materials and Components Research Division, Superintelligence Creative Research Laboratory, Electronics and Telecommunications Research Institute (ETRI), Daejeon, 34129, Republic of Korea*

ARTICLE INFO

Communicated by Jang-Kyo Kim

Keywords:

5G antenna
3D printing
Circular polarization
Sequentially rotated phased feed network
Small satellite
Low Earth Orbit

ABSTRACT

This paper presents the design, fabrication, and testing of a high-gain compact 2×2 circularly polarized patch antenna array using 3D printing technology for small satellite 5G communication at 28 GHz. The proposed antenna demonstrates high efficiency and a low profile, addressing the limitations in design flexibility associated with traditional PCB fabrication methods. The 2×2 array configuration, incorporating via fences, coaxial vertical feedlines, and a sequentially rotated phased feed network, enhances the antenna's bandwidth and axial ratio bandwidth while maintaining compactness, crucial for space-constrained satellite applications. Simulations optimized key antenna parameters, including reflection coefficient, gain, and axial ratio. Measurement results validated the simulations, showing an impedance bandwidth of 6.8 GHz and an axial ratio bandwidth of 3.1 GHz, with a peak gain of 6.33 dB. Thermal cycling and electrical tests ensured the antenna's durability in space environments, demonstrating its potential for satellite use. These results indicate that 3D-printed antennas offer advantages in performance, cost, and manufacturing flexibility for satellite communication applications.

1. Introduction

The market for small satellites is changing rapidly because they are a cost-effective and multi-purpose solution. The international market of small satellites grew to approximately 4.91 billion USD in 2023 and is expected to grow to 18.4 billion USD by 2032, with a compound annual growth rate of 15.8% [1]. In particular, the use of CubeSats has been increased in various fields such as earth observation, communications, and scientific research for low-earth orbit (LEO) missions due to their rapid production and low cost [2,3].

LEO small satellites require antennas with a high gain and a small size to be operated in the limited power environments. High-efficiency antennas have been studied in various directions, including electromagnetic bandgap (EBG) structures [4], Huygens source antennas [5], dipoles with backed cavities [6], and metasurface structures [7–10]. However, although these antennas improve the gain and circular polarization (CP) characteristics, they are unsuitable for small satellites. These structures are large, or their structural stability in space and launch environments is inadequate due to structures such as air gaps. On the other hand, among planar antennas, patch antennas are mainly used in the production of small satellites because of their low profile, light

weight, and easy assembly. However, patch antennas have a narrow bandwidth because of their structural characteristics [11]. This drawback makes transmission and reception difficult when the Doppler effect generates a frequency shift [12–15]. To overcome this problem, a patch antenna structure capable of producing a high bandwidth must be designed.

In a satellite communication environment, maintaining the communication status between the satellite and the ground, that is, the alignment status, is important. Satellites at the LEO positions are likely to have a horizontal alignment status that does not match with the ground base station due to their fast orbital speeds [14]. Therefore, CP is considered an important element for communication independent of the rotational state of the satellite [3]. Optimizing the high gain and the low axial ratio (AR) for the operating frequency is important for designing CP antennas. However, it isn't easy to match the gain bandwidth and the axial ratio bandwidth within the same range. Therefore, the main goal of the research on CP antennas is to improve antenna performance through design improvement and changes in the fabrication method [16,17]. The antenna array arrangement effectively improves the directivity and gain of the antennas, and may increase the narrow bandwidth of the patch antennas [18]. In CP communications, an AR value of less than 3 dB

* Corresponding author.

E-mail addresses: jengsu@etri.re.kr (J. Yoo), mlee@etri.re.kr (M.L. Lee), jullios@etri.re.kr (Y.S. Yang).

is required. However, in satellite communications, an AR value of less than 1.5 dB is required by the MIL-STD-188-164A standard of the U.S. Department of Defense, considering the mutual interference between satellites and the communications environment [19].

In this study, as a CP antenna array design, we propose a shape in which the phase of the signal input to each antenna element is different, thereby enhancing the CP characteristics. This shape allows the direction of the total electric field vector to rotate according to the phase to create the CP characteristics. To this end, the feed input to each element may be put in through a separate coaxial cable [17,20,21]. Because this method is structurally large and complex, requiring additional circuit design to control the input to each feed, it is unsuitable for small satellites. Therefore, in the design of this study, we used a one-port input and a method of inputting it to each antenna element with a different phase through the feed network. The feedlines connected to each antenna element must have different path differences to create a phase difference in this structure. For example, two feedlines must have a path difference of $\lambda/4$ to make the phase difference of the two feedlines 90° . In many studies on producing antenna arrays, straight feedlines are designed to pursue simplicity in feed network design [22,23]. However, this straight structure causes resistive loss and an increase in the area of the feed network due to an increase in the length of the transmission line [24]. As an alternative, using a sequentially rotated (SR) phased feed network has been proposed [16,25–32]. This SR phased feed network has a form in which the feedline is arranged in a circular shape at the center of the array, rather than a straight line, and is operated such that the signal transmitted through a single circular feedline is distributed to each port according to the path difference, that is, the phase. Therefore, the SR feed network structure has the advantage of reducing the area and resistive loss compared to the linear feed network, and ultimately increasing the axial ratio bandwidth (ARBW) and impedance bandwidth.

The printed circuit board (PCB) fabrication method is mainly used in conventional patch antenna fabrication. Since there may be a difference in performance between the design and the actual fabrication result, a continuous design change process is required to produce the final result. These design changes and fabrication processes require a lot of time and cost for the PCB fabrication method. In addition, the multilayer structure [17,33] in which the feed is arranged in a different layer for high gain characteristics causes an increase in process steps in this method. Therefore, the microstrip patch antenna structure, where the antenna element and feedline are arranged on the same surface, is generally employed to minimize the cost and manufacturing process [16,34,35]. This structure causes mutual interference between the feedline and the antenna and spurious radiations [36,37].

The application of 3D printing in antennas has been attempted in various directions [38,39]. The fabrication of Luneburg lens structure that can increase the gain value of the antenna by printing dielectric materials [18,40], the fabrication of a horn antenna through metal printing [41], and the fabrication of antennas through metal printing on a structure [42] have been proposed. Since antenna applications of this type mainly allow for the printing of only a single material, the structures that can be fabricated are limited. However, the emergence of multi-material 3D printers capable of printing dielectrics and conductors simultaneously has made it possible to overcome the limitations in fabrication and design [43–47]. This printing method allows for the application of microvias, via fencing, and multilayer fabrication used in conventional PCB fabrication without additional operations such as separate drilling [48].

In space technologies, including satellite systems, electronic components must be evaluated for their reliability under the harsh conditions of the space environment. These environmental factors encompass the entire mission profile from the launch phase and orbital deployment to prolonged exposure in space. During launch, satellite structures are subjected to severe mechanical and thermal stress, including random vibrations, high-frequency and low-frequency oscillations, all of which

can impose significant mechanical loads on structural interfaces and mounted components [49–52]. Moreover, the extreme thermal fluctuations experienced after deployment, ranging from intense heat to cryogenic temperatures, can introduce substantial thermo-mechanical stress to onboard devices. Such stress may lead to deformation or delamination in polymer-based materials, making rigorous environmental testing critical for space qualification [50,53]. Recent advancements in 3D printing technology have enabled the fabrication of mechanically robust structures using polymeric materials, which can better withstand thermo-mechanical stresses encountered in space applications [54]. In this study, we conducted thermal cycling tests to examine the thermal resilience of the antenna structure, while comprehensive thermo-mechanical testing is planned as part of our future work.

This study presents a 28 GHz CP 2×2 patch antenna array structure fabricated using 3D printing technology. The printing material used in the present study has a loss tangent value of 0.016, which is larger than 0.001 (Duroid 5880) [29] and 0.0009 (Rogers 5880) [5] of the PCB materials. Thus, the resulting signal transmission loss is relatively large [55]. We aimed to overcome this drawback by fabricating structures such as coaxial feedline, SR feed network, and via fencing through 3D printing. In this study, we separated the feed network and patch radiating elements and improved signal output through via fencing. 3D printing simplified the multilayer structure fabrication process without a post-process, even though the feed network was separated from the patch elements. Through space environment tests based on the European Cooperation for Space Standardization (ECSS), an evaluation reference for space devices, we demonstrated that the 3D printing material can be used for space electronic devices. We measured the fabricated antenna's performance, demonstrating that it met the requirements for small satellite communications.

2. Design of array antenna

2.1. Patch element design

2.1.1. Single element

The characteristics of a patch antenna are determined by geometrical parameters such as the patch's width, length, and substrate thickness. A patch antenna's resonant frequency f_0 is expressed as follows.

$$f_0 = \frac{c}{2L\sqrt{\epsilon_r}} \quad (1)$$

Here, c is the speed of light, L is the length of the patch, and ϵ_r is the permittivity of the substrate. The width of the patch affects the bandwidth and gain, and generally, as the width increases, the gain and bandwidth tend to increase, and as the length increases, the frequency tends to decrease [11,56].

The CP radiation characteristics of a CP antenna are confirmed through the AR. The AR is calculated by the following equation through the electric field magnitude of the co-polarization ($|E_{co-pol}|$) and cross-polarization ($|E_{x-pol}|$) in CP oscillation [57].

$$AR(dB) = 20 \log \left(\frac{|E_{co-pol}| + |E_{x-pol}|}{|E_{co-pol}| - |E_{x-pol}|} \right) \quad (2)$$

The polarization of the electric field is not a perfect circle but an ellipse, and making this ellipse a circle with an AR value close to 0 dB is important for implementing CP communications. The antenna fabricated in this study was designed to have an AR value of 1.5 dB or less, which is the AR criterion for space communications [19].

Fig. 1 shows the configuration of a single patch antenna. The CP patch antenna is mainly designed as a square patch antenna with the corners truncated at 45° , with a length S [3]. The square patch's theoretical value of the length L is determined according to the frequency in (1). In the CP patch antenna, the length L was determined as an optimal

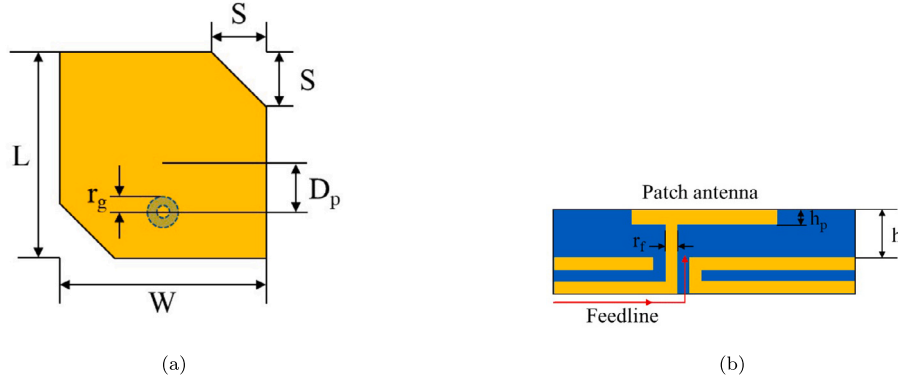


Fig. 1. Geometries of single patch coaxial feed antenna. (a) Top view and (b) Cross section view ($L = W = 2.96$ mm, $S = 0.44$ mm, $D_p = 0.60$ mm, $h = 0.28$ mm, $h_p = 0.03$ mm, $r_g = 0.405$ mm, and $r_f = 0.20$ mm).

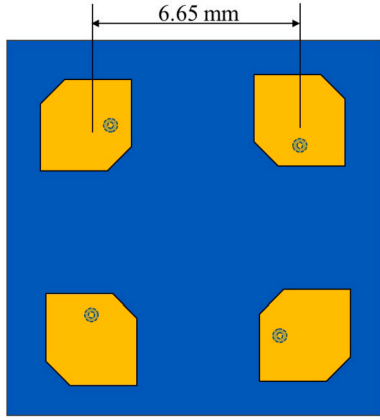


Fig. 2. Configuration of 2×2 patch antenna array arrangement.

value through simulation, considering the impedance change due to the truncated area. To reduce spurious radiation caused by the feedline during signal oscillation in the fabricated patch element, the antenna was vertically connected with the feedline at a position away from the center of the patch by a length D_p in the form of a vertical coaxial feedline, rather than a microstrip feedline [36,37,58]. The vertical feedline was fabricated in a form in which the periphery of the vertical feedline is surrounded by a cylindrical grounded via to reduce radiation loss.

2.1.2. 2×2 patch antenna array

The narrow range of the total impedance bandwidth (IBW) and the ARBW of a patch antenna makes it difficult to use the patch antenna for satellite communications. The antenna array alignment is mainly used to increase the antenna's bandwidth, through which the antenna's bandwidth is expanded and the gain characteristics are enhanced [3]. Such an array alignment can enhance the CP characteristics by amplifying the electric field radiated from each element through constructive interference. It significantly increases the ARBW, which is inevitably limited by structural factors in a single patch. The optimized single patch antenna shape shown in Fig. 1a was arranged in the array shape of Fig. 2. The distance between patch elements with high radiation efficiency in the array method has a theoretical value of $0.7\lambda_0$ when only the patch elements are considered [59]. This distance was determined to be 6.65 mm ($0.64\lambda_0$), a value optimized through simulation by reflecting the dielectric loss and the entire antenna structure. Here, λ_0 is the free space wavelength. Each patch was rotated 90° to enhance the CP characteristics [31].

Table 1
Geometrical parameters of the SR feed network.

Number	Width w (mm)	Length l (mm)	Impedance Z (Ω)
1A	0.400	0.995	37.88
1B	0.568	0.795	33.69
2	0.105	1.583	117.28
3	0.693	1.590	16.80
4	0.255	1.583	55.36
5	0.402	1.590	35.85
6	0.259	1.583	54.46
7	0.089	1.590	148.79
8	0.259	1.583	54.46
s	0.010	0.205	-

2.2. Design of the feed network

2.2.1. SR phased feed network

To transmit signals of different phases with the same size to each patch element, an SR feed network, as shown in Fig. 3a, was fabricated. The circular feed elements Z_1 (Z_{1A} and Z_{1B}), Z_3 , Z_5 , and Z_7 were designed and arranged in the form of an arc with reference to the same center point. Through this, the signal is transmitted to each port, that is, the patch antenna element, through the linear feed elements Z_2 , Z_4 , Z_6 , and Z_8 . In this feed network, the phase delay between the individual ports is 90° , which means that each element of the circular feedline at the center should have an electrical length of $\lambda_g/4$ (1.62 mm), where λ_g is the guided wavelength in the dielectric material. The linear line elements Z_2 , Z_4 , Z_6 , and Z_8 are quarter-wavelength transformers. Fig. 3b shows the configuration of the equivalent circuit of the feed network. Since a signal of the equal power ($P_{in}/4$) must be input to each port, the impedance of each feedline element was set through simulation.

First, according to the basic transmission line theory regarding the power divider, the impedance ratio at each branch point was calculated as follows, according to the power distribution ratio.

$$Z_{in1} = \frac{1}{3}Z_2, \quad Z_{in2} = \frac{1}{2}Z_4, \quad Z_{in3} = Z_6 \quad (3)$$

Based on this equation, the initial impedance value of the feed network elements was set. Since this initial value reflected power dividing through impedance only, the geometry was optimized through simulation, considering the phase difference [16,23]. The phase difference between Ports 2, 3, 4, and 5 should be 90° , which was implemented through the path difference of the feedlines. A stub (Z_s) was added to adjust the phase and impedance finely. Considering all of these conditions, the parameters of each transmission line were obtained as shown in Table 1. The SR feed network designed in this way has a size of $0.41\lambda_g \times 0.41\lambda_g$, which is as small as $0.35\lambda_g \times 0.35\lambda_g$ which is the size

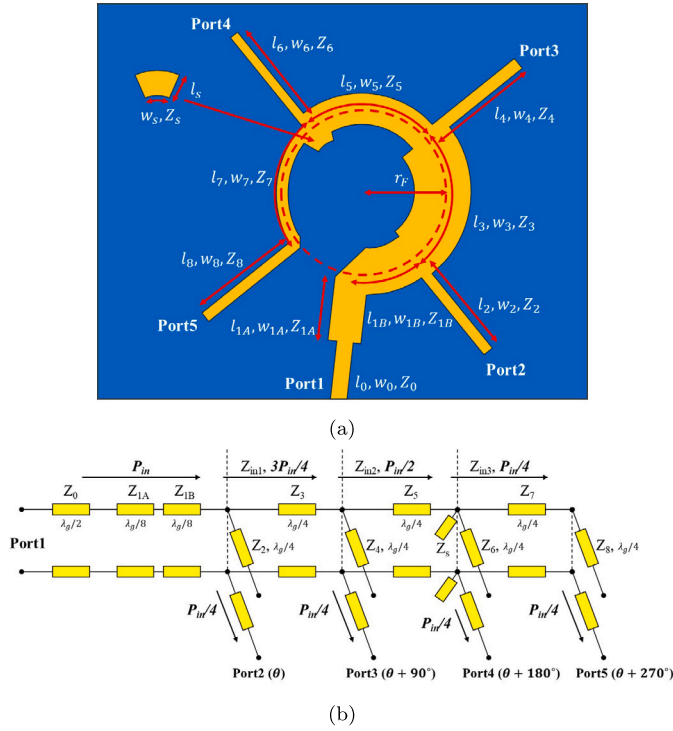


Fig. 3. SR phased feed network: (a) Geometry and (b) Equivalent circuit model: ($w_{1A} = 0.400$, $w_{1B} = 0.568$, $w_2 = 0.105$, $w_3 = 0.693$, $w_4 = 0.255$, $w_5 = 0.402$, $w_6 = 0.259$, $w_7 = 0.089$, $w_8 = 0.259$, $w_s = 0.010$, $l_{1A} = 0.995$, $l_{1B} = 0.795$, $l_2 = l_4 = l_6 = l_8 = 1.583$, $l_3 = l_5 = l_7 = 1.590$, $l_s = 0.205$, and $r_F = 1.013$) mm, ($Z_0 = 50$, $Z_{1A} = 37.88$, $Z_{1B} = 33.69$, $Z_2 = 117.28$, $Z_3 = 16.80$, $Z_4 = 55.36$, $Z_5 = 35.85$, $Z_6 = 54.46$, $Z_7 = 148.79$, and $Z_8 = 54.46$) Ω .

of the SR feed network in a study on miniaturization of a 2×2 patch antenna array [16].

2.2.2. Via fencing for decreasing feedline signal loss

In the design of electronic devices, a via fence connected to the ground is arranged around the conducting feedline to reduce the radiated loss [60,61]. Among such electronic devices, when a radio frequency device such as an antenna is designed, radiation from the feedline rather than the antenna may cause signal interference between lines and reduce efficiency. A via fence was designed to reduce these problems and transmit signals to the waveguide structure between the feedline and the fence [62]. In the via fabrication process of PCBs, vias used only in specific layers, such as buried vias, blind vias, and staggered microvias, are difficult to fabricate. Through-hole vias are mainly used, which reduces the degree of freedom in antenna design. On the contrary, by introducing a 3D printing method in the antenna fabrication, vias with structures such as plate or cylinder shapes were fabricated without additional drilling, regardless of the layer's position.

For the horizontal feedline, rather than continuously arranging cylindrical vias on the PCB, a vertical plate-shaped via fence was arranged, a structure that is as close to a waveguide shape as possible. A waveguide similar to a coaxial cable was fabricated when the vertical feedline was fabricated to connect the layers. Through simulation, the waveguide was designed as a coaxial input cable with a central feedline radius of 0.10 mm, a metal ground shielding cylinder radius of 0.405 mm, and an impedance of 50 Ω .

Fig. 4 shows the simulation results of S-parameter and phase difference when a via fence is present or absent in the feed network, respectively. In Figs. 4a and 4b, it was confirmed that when the via fence was present, the same level of power was transmitted and the phase difference was also close to 90° in the frequency range from 27 GHz to 29 GHz. Figs. 4c and 4d show that when the fence was absent.

Despite that, the phase difference between individual ports was about 90° , it was not uniform, and the power difference between individual ports was large in the frequency range. This signal imbalance may be due to the above-described signal interference between feedlines and radiating loss. These results indicate that the bandwidth was widened by via fence.

2.2.3. Assembly of antenna elements for array displacement

Fig. 5 shows the overall antenna structure in which the optimized antenna array elements, SR feed network, and via fence structures are connected with feedlines. Each patch radiating element is connected to an SR feed network, and this feedline stably transmits signals through the via fence structure. The thicknesses of the layers in which each structure was located were as follows: $h_1 = 0.28$, $h_2 = 0.23$, $h_3 = 0.23$, $h_4 = 0.40$, and $h_5 = 0.15$ mm. The thicknesses of the remaining printed horizontal metal layers were all 0.05 mm. Since the fabricated antenna was connected to an external signal source through a horizontal connector, the feedline of the bottom layer was exposed as a microstrip line.

2.3. Antenna design: simulation results

Fig. 6 shows the results of simulating the performance of a single patch antenna and a patch antenna array. The IBW value corresponding to $S_{11} \leq -10$ dB of a single patch was 2.05 GHz, the gain value at the target frequency of 28 GHz was 5.36 dB, and the bandwidth was 3.60 GHz. About the CP characteristics, the ARBW corresponding to $AR \leq 3$ dB was 0.39 GHz, which was narrower than the IBW, and the AR value at the target frequency also failed to satisfy the AR value of less than 1.5 dB recommended for space communications.

In the case of the patch antenna array, the AR and gain characteristics were improved. The IBW was 6.20 GHz, the ARBW was 3.49 GHz, the gain was 9.31 dB at 28 GHz, and the gain bandwidth was 2.97 GHz, which are increased values compared to the single patch antenna. The S-parameter value at the target frequency of 28 GHz also decreased from -11.47 dB to -13.87 dB, indicating reduced signal loss.

2.3.1. Far field simulation

To use the designed antenna as a space antenna, a goal was set for the range of gain and AR angular width to cover $\theta = \pm 10^\circ$ based on the vertical direction [16]. Figs. 7a and 7b show the gain radiation patterns of a single patch antenna and a patch antenna array. The radiation pattern of the single patch antenna was symmetrical to the two ϕ planes and had a gain deviation of below 3 dB. In the patch antenna array, it was confirmed that the radiation direction was not vertical but tilted in the $\theta = 5^\circ$ direction when $\phi = 0^\circ$. Nevertheless, since the gain deviation in the $\pm 10^\circ$ range was less than 3 dB, it was judged that stability can be guaranteed even in long-distance communications.

Figs. 7c and 7d show the AR radiation patterns of a single and a patch antenna array. Unlike its gain characteristics, the single patch antenna has a narrow angular width, so only a part of the region of $\theta = \pm 10^\circ$ exhibited a gain deviation value of less than 3 dB, making it limiting stable CP signal radiation. The patch antenna array showed an AR value of less than 1.5 dB in the entire region of $\theta = \pm 10^\circ$. These results imply that an antenna that satisfies the 1.5 dB value required for satellite communications can be implemented through the array structure.

3. Experiment results

3.1. Qualification of 3D printing materials for space environment

We herein demonstrate a method for fabricating antenna electronic devices by simultaneously printing dielectrics and conductors, which can replace the PCB fabrication method. The equipment used for 3D printing in this study was DragonFly 3D printer (Maximum printing size: 160 mm \times 160 mm \times 3 mm, Minimum pixel width $w = 36$ μ m, and Minimum layer thickness $t = 10$ μ m) (NanoDimension, Israel), and

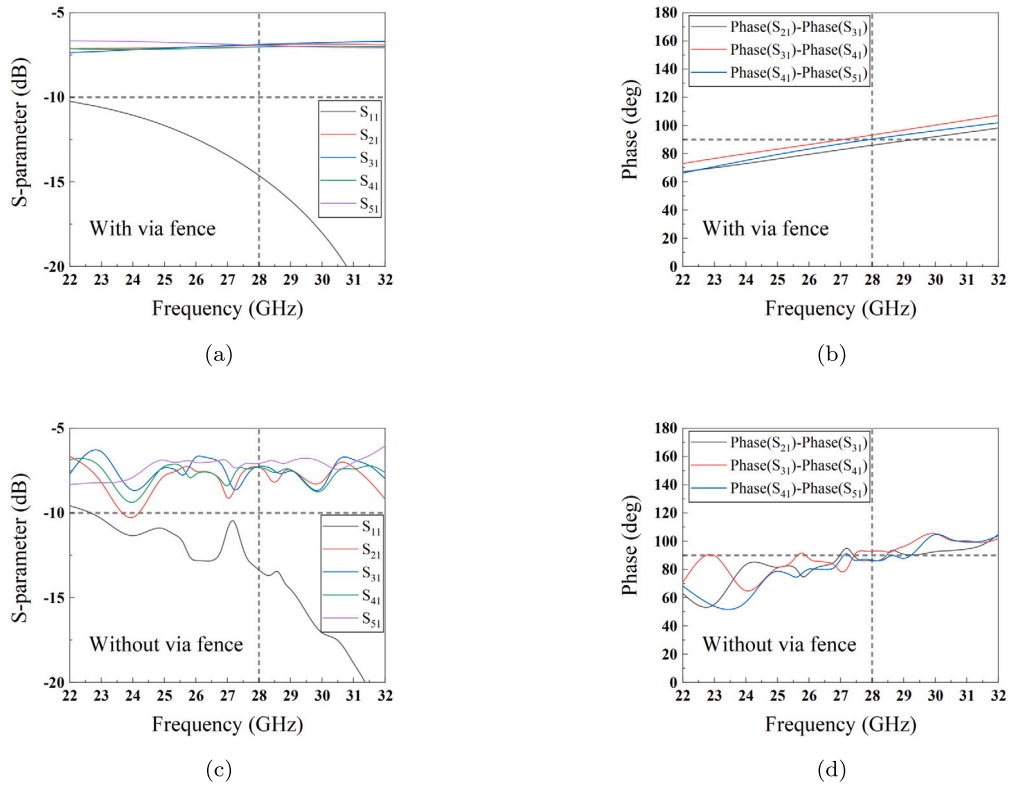


Fig. 4. Simulated performance of feed network: (a) S-parameters with via fences, (b) Phase difference of the signals between the output ports with via fences, (c) S-parameters without via fences, and (d) Phase difference of the signals between the output ports without via fences. (For interpretation of the colors in the figure(s), the reader is referred to the web version of this article.)

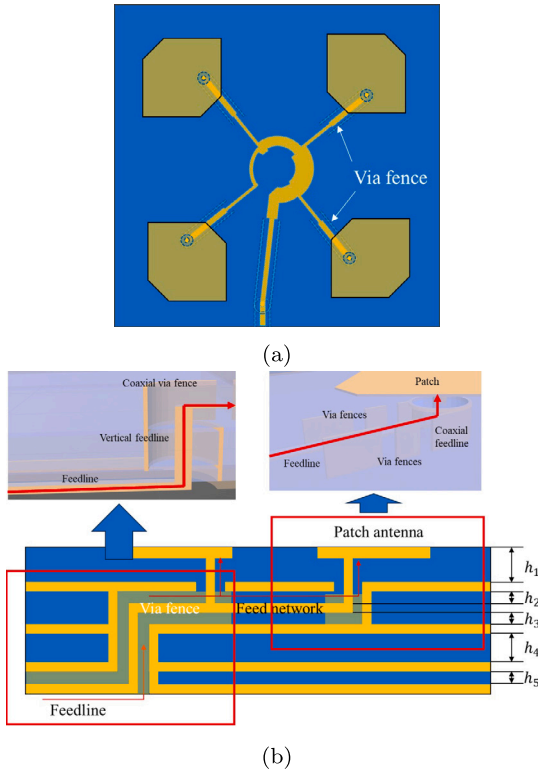


Fig. 5. Geometries of patch antenna array with sequentially rotated phase feed network: (a) Top view and (b) Cross section view: ($h_1 = 0.28$, $h_2 = 0.23$, $h_3 = 0.23$, $h_4 = 0.40$, and $h_5 = 0.15$) mm.

acrylate series ink ($\epsilon_r = 2.83$, $\tan\delta = 0.016$, and Maximum curing temperature $T = 180\text{ }^\circ\text{C}$) was used as a dielectric, and silver nano-particle ink was used as a conductor [55]. This inkjet printing method creates a PCB structure by spraying conductive and dielectric ink through hundreds of nozzles.

Unlike the Earth’s environment, the LEO environment undergoes extreme temperature changes from 380 K to 240 K, depending on the presence or absence of sunlight in a vacuum environment [63]. Therefore, materials that cause minimal environmental damage or performance degradation should be used when designing electronic devices for artificial satellites. Its durability and chemical stability in the space environment must be confirmed to confirm the possibility of using the 3D printing material used in this study as a satellite antenna.

An outgassing test is a test to examine the possibility that gases or organic molecules on the surface or inside of a material may be released in a vacuum or high-temperature environment to cause deformation of the material or damage to surrounding components. In the present study, we conducted a test evaluation to examine whether the outgassing conditions are satisfied in a space environment based on the ECSS-Q-ST-70-02C of the European Space Agency using the Collected Volatile Condensable Materials System (VMT, Korea) equipment [64]. The evaluation items for measuring the mass changes were the total mass loss (TML), collected volatile condensable materials (CVCM), and recovered mass loss (RML). Regarding the measurement environment for each evaluation item, the TML of a specimen is measured for 24 hours in a high-vacuum chamber at 125 °C. The CVCM of a collector plate is measured by placing it in a chamber with a specimen in a high-vacuum environment at 125 °C. The RML is measured 24 hours in a thermo-hygrostat chamber at 23 °C and 55% relative humidity. The results of this outgassing test are summarized in Table 2. It was confirmed that all test results for each item met the material outgassing evaluation criteria.

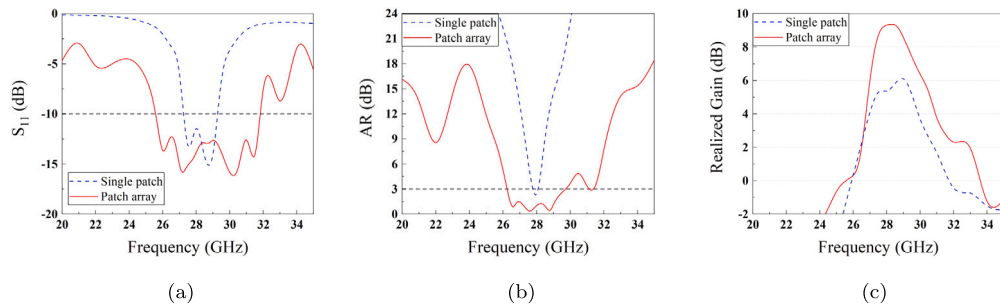


Fig. 6. Comparison of the simulated performance between single patch antenna and patch antenna array: (a) Reflection coefficient, (b) AR, and (c) Gain.

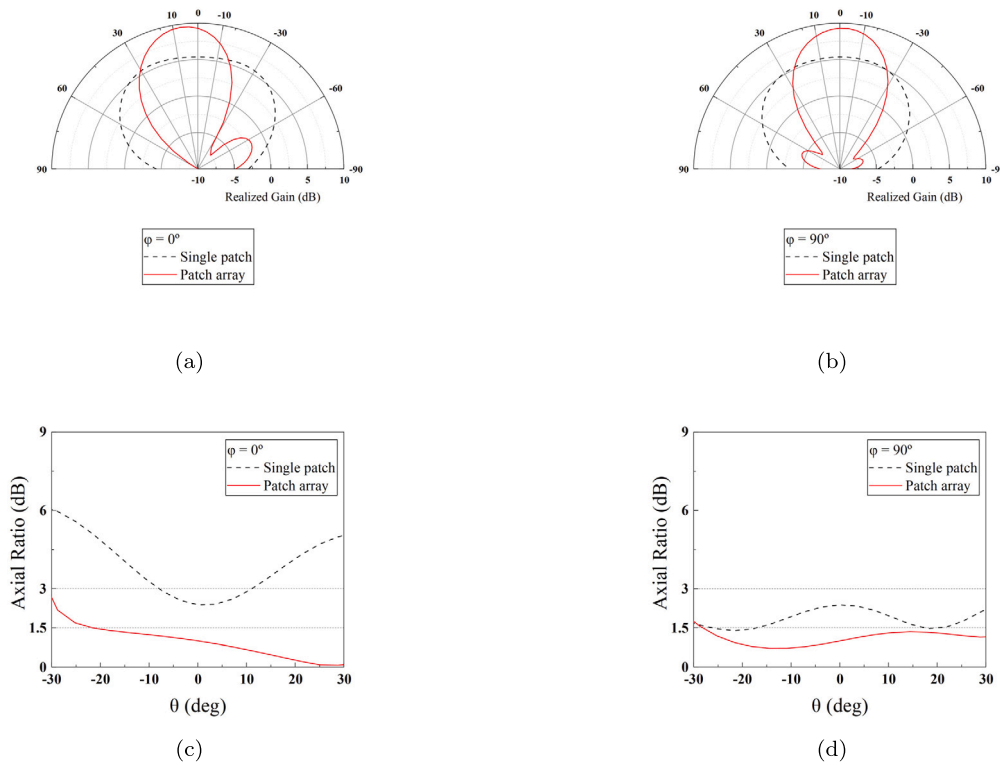


Fig. 7. Simulated gain radiation patterns (a) in the $\phi = 0^\circ$, and (b) in the $\phi = 90^\circ$ and axial ratio radiation patterns (c) in the $\phi = 0^\circ$, and (d) in the $\phi = 90^\circ$ of single patch antenna and patch antenna array.

Table 2
Comparison of outgassing ECSS-Q-ST-70-02C standards and 3D printed patterns test results.

Test	Measurement result	ECSS-Q-ST-70-02C standard	Test result
TML	0.580%	< 1.0%	Fine
CVCM	0.003%	< 1.0%	Fine
RML	0.320%	< 1.0%	Fine

Space environment verification of the printing materials was performed based on the PCB material evaluation standard document ECSS-Q-ST-70-10C [65]. The evaluation items were the interlayer insulation, intralayer insulation, and continuity, which were configured to confirm the electrical characteristic changes in the space environment.

Fig. 8 shows the specimens fabricated through 3D printing to verify the electrical characteristic changes in the space environment. Fig. 8a shows a pattern for verifying the intralayer insulation, and the pattern consisted of parallel lines that were not electrically connected and were arranged with a spacing of 0.5 mm on the same plane. Fig. 8b shows a pattern for verifying the interlayer insulation, and the pattern consisted

of two parallel metal plates with a spacing of 2 mm that were not electrically connected and were arranged in intervals of 0.5 mm. Through these two patterns, the insulation performance of the dielectric used in the printing process can be verified. Fig. 8c shows a 52-daisy chain via pattern. The electrodes at both ends were electrically connected to the vias with a diameter of 1.8 mm to confirm the possibility of abnormal electrical conductivity.

The electrical and thermal characteristic verification patterns are shown in Fig. 8. The temperature range was from -60°C to 140°C , and the number of thermal cycles was 200. The thermal test was applied using a TCC-150 thermal cycle chamber (Espec, Japan). The electrical characteristics of the patterns and their changes before and after the environmental change were evaluated.

For the insulation patterns shown in Figs. 8a and 8b, the insulation resistance and withstanding voltage were measured using a DU-3315 Hi-Pot Tester (Delta United, Taiwan). The resistance between the two electrodes was measured after a voltage of 500 V had been applied to measure the insulation resistance. The measurement results of both the intralayer and interlayer patterns before and after the thermal cycling were above $10^5\ \text{M}\Omega$. Two withstanding voltage tests confirmed that the

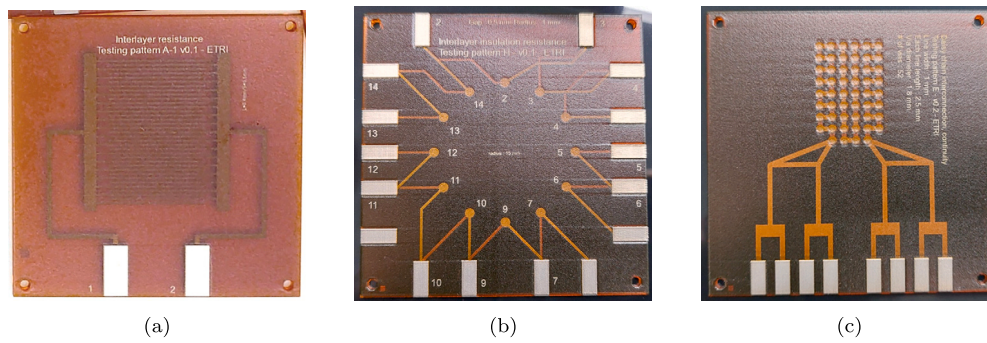


Fig. 8. The printed space environment test patterns for electrical properties of (a) intralayer insulation, (b) interlayer insulation, and (c) Daisy chain continuity.

Table 3
Comparison of outgassing ECSS-Q-ST-70-10C standards and 3D printed patterns test results.

Test	Specification	ECSS contents	ECSS standards	Measurement	Evaluation
Insulation before thermal cycling	Intralayer	7.2.8.2	$> 10^4 \text{ M}\Omega$	$> 10^5 \text{ M}\Omega$	Fine
		7.2.8.4	$< 100 \mu\text{A}$ at $500 \text{ V}_{\text{rms}}$	$10 \mu\text{A}$	Fine
	Interlayer	7.2.8.3	$> 10^5 \text{ M}\Omega$	$> 10^5 \text{ M}\Omega$	Fine
		7.2.8.4	$< 100 \mu\text{A}$ at $500 \text{ V}_{\text{rms}}$	$11 \mu\text{A}$	Fine
Insulation after thermal cycling	Intralayer	7.5	$> 10^3 \text{ M}\Omega$	$> 10^5 \text{ M}\Omega$	Fine
		7.5	$< 100 \mu\text{A}$ at $500 \text{ V}_{\text{rms}}$	$13 \mu\text{A}$	Fine
	Interlayer	7.5	$> 10^4 \text{ M}\Omega$	$> 10^5 \text{ M}\Omega$	Fine
		7.5	$< 100 \mu\text{A}$ at $500 \text{ V}_{\text{rms}}$	$5 \mu\text{A}$	Fine
Conductivity before thermal cycling	Daisy chain	7.2.8.5, 7.2.8.6	Dispersion $< 10\%$	0.40%	Fine
Conductivity after thermal cycling	Daisy chain	7.2.8.5, 7.2.8.6	Dispersion $< 10\%$	0.40%	Fine

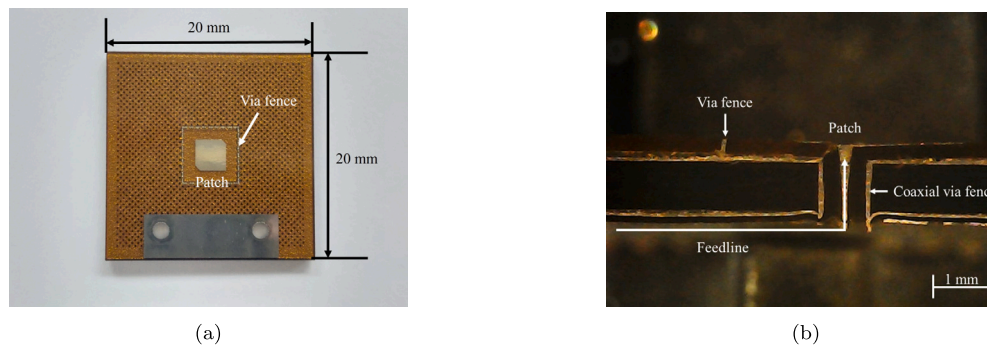


Fig. 9. Photograph of 3D printed single patch antenna: (a) Top view. (b) Cross-section view.

leakage current of the test patterns was under $100 \mu\text{A}$ at $500 \text{ V}_{\text{rms}}$ with 50 Hz. The measurement results satisfied the criteria in the thermal cycling test, as summarized in Table 3.

In Fig. 8c, the conductivity of the electrical continuity test pattern was shown. The average measured resistance was 0.92Ω and the dispersion was 0.40% before the thermal cycling, and was 0.96Ω and the dispersion was 0.05% after the thermal cycling. In addition, the resistance change rate before and after the thermal cycling was found to be 4.35%. When used as an electrically conductive element, the electrical conductivity can be maintained even under thermal changes in the space environment.

Through these verification processes in the electrical and chemical space environments, we confirmed that the antenna devices fabricated from the 3D printing materials can be used in the space environments.

3.2. Fabricated antenna measurements

3.2.1. 3D printed antennas

Fig. 9 shows a 3D printed single patch antenna. The antenna was fabricated with a size of $20.00 \text{ mm} \times 20.00 \text{ mm} \times 1.55 \text{ mm}$ and in-

cluded two holes for fixing and connecting a connector. In Fig. 9a, a metal plane was disposed on the top portion to connect with the ground plane of the connector as widely as possible.

Fig. 9b shows the antenna cut vertically to confirm the internal print status and the presence of feedline connections. Both the thickness of the patch and the feedline satisfied the design size. Although the structure may not be considered identical to the design due to the characteristics of the inkjet printer, the electrical connection between the patch and the feedline and the coaxial feedline and cylindrical shielding structure were stably fabricated.

Fig. 10 represents the patch antenna array fabricated by using 3D printing and designed in Fig. 5. The antenna was fabricated with a size of $20.00 \text{ mm} \times 24.00 \text{ mm} \times 1.56 \text{ mm}$ and included two slots for fixing and connecting a connector. Through the vertical cross-section of Fig. 10b, the printed shape of the electrically connected metal lines leading to the vertical via feedline, coaxial ground shielding, and feed network was formed as designed. In Fig. 10c, the physical contact was made between the connector and the microstrip line of the bottom layer so that the signals could be transmitted. The SR feed network in Fig. 10d

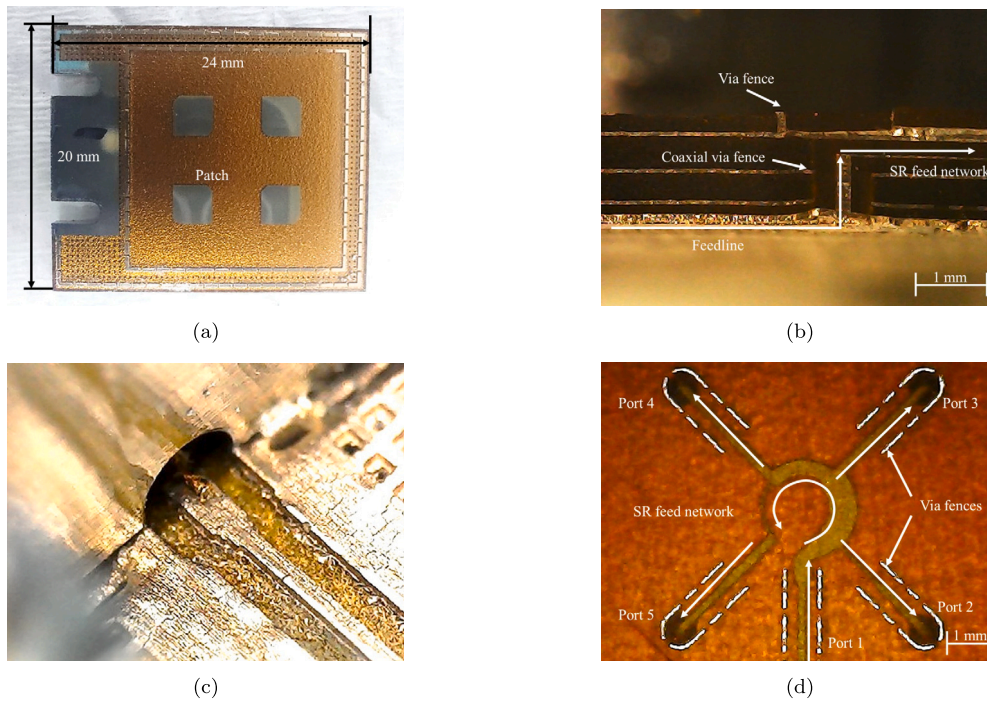


Fig. 10. Photograph of 3D printed patch antenna array: (a) Top view, (b) Cross section view, (c) Magnification view of the connection between microstrip line and contact pin, and (d) The SR feed network.

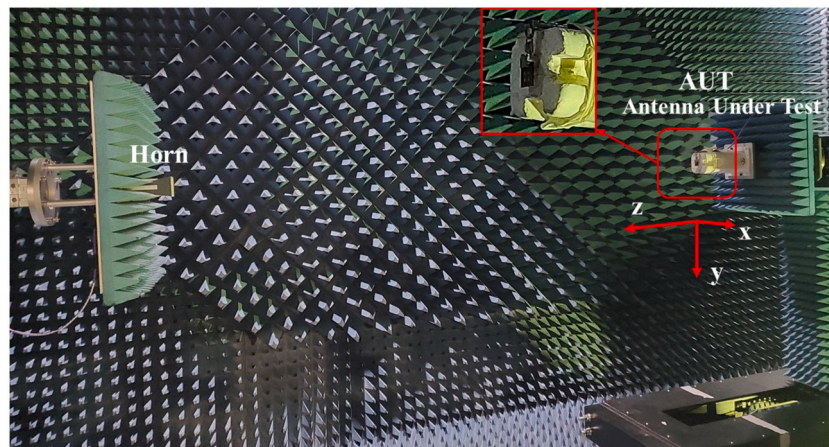


Fig. 11. Far-field measurement in a fully mmWave anechoic chamber with experimental setup system.

was electrically connected to each antenna element, and the circular power divider structure in the center was fabricated as designed.

3.2.2. Measurements of antenna performance

Fig. 11 shows the mmWave anechoic chamber (Korea Radio Promotion Association, Korea) for far field measurement of the fabricated antenna. The chamber was electromagnetically isolated from the outside, and the polarization and radiation pattern were measured through the rotation angle and position change with respect to the linearly polarized horn antenna. In the far field analysis, the radiated power and polarization were measured to the vertical and horizontal axes, that is, at $\phi = 0^\circ$ and $\phi = 90^\circ$ by connecting the network analyzer (Agilent E8362C, USA) to the fabricated antenna and the horn antenna. The AR radiation pattern, which determines the gain and CP performance, was measured using the measurement results.

Fig. 12 shows the results of measuring the radiation performance of each fabricated single patch antenna and patch antenna array. The IBW value of the single patch was 8.86 GHz, and the gain value at the

target frequency of 28 GHz was -1.31 dB with a bandwidth of 4.5 GHz, indicating that the antenna radiation performance was lower than the predictions by the simulation. In addition, in this study, the AR value, which is important in the CP characteristics, was found to be 3.30 dB at the target frequency of 28 GHz, confirming that CP communication was impossible.

Compared to the single patch, the patch antenna array exhibited improved AR and gain characteristics with an IBW of 8.00 GHz, an ARBW of 3.10 GHz, a gain of 6.44 dB at 28 GHz, and a gain bandwidth of 2.70 GHz, as the simulation results shown in Fig. 6, demonstrating performance that allows the patch antenna array to function as a CP antenna. This improvement in bandwidth and radiation performance suggests that the antenna arrangement in an array structure could be a method for improving performance despite the insufficient performance of individual antennas and that the array structure can be used for satellite communications by reducing the AR value to less than 1.5 dB.

Figs. 13a and 13b show the radiation patterns for the gain of a single patch antenna and a patch antenna array. The single patch antenna

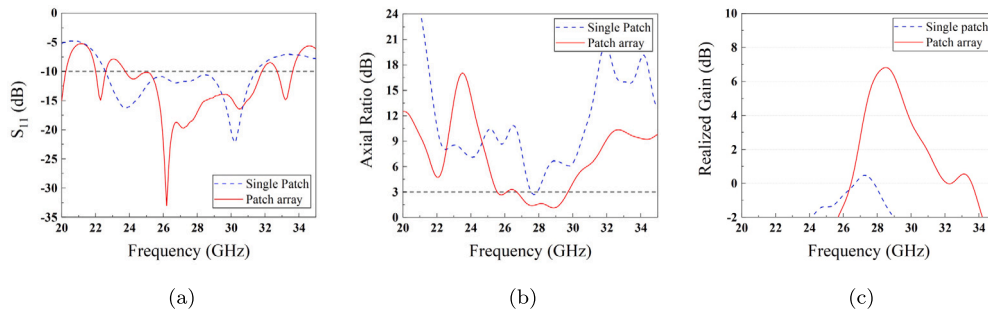


Fig. 12. Comparison of the measured performance between single patch antenna and patch antenna array: (a) Reflection coefficient, (b) AR, and (c) Gain.

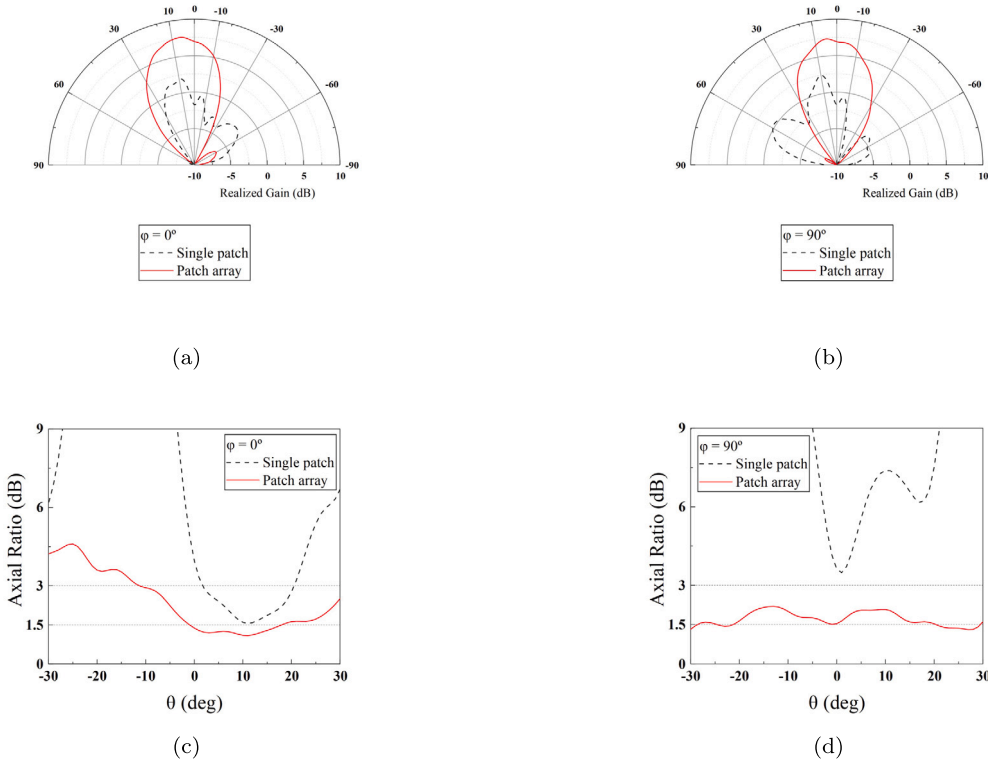


Fig. 13. Comparisons of measured gain radiation patterns (a) in the $\phi = 0^\circ$, and (b) in the $\phi = 90^\circ$ and axial ratio radiation patterns (c) in the $\phi = 0^\circ$, and (d) in the $\phi = 90^\circ$ of single patch antenna and patch antenna array at 28 GHz.

exhibited a low radiation efficiency value, which tended to be lower than the simulation value. In the patch array antenna, the deviation of gain value in the region of $\theta = \pm 10^\circ$ at the target frequency of 28 GHz was less than 3 dB, as predicted in the simulation. The angular width was 35.5° and 35.7° at $\phi = 0^\circ$ and $\phi = 90^\circ$, respectively. As predicted from the simulation in Fig. 7, the CP characteristics of the single patch antenna in Figs. 13c and 13d show the angular width of gain and AR narrower than $\theta = \pm 10^\circ$. This indicates that the single patch element structure is difficult to serve as a CP antenna. In the patch array antenna, the angular width of less than 3 dB was found to be 43.6° and 95.5° at $\phi = 0^\circ$ and $\phi = 90^\circ$, respectively, and the values were less than 1.5 dB at some angles. This demonstrates the radiation performance improvement enabled by the array structure.

Figs. 14a and 14b show the gain radiation patterns at 27, 28, and 29 GHz. At 27 GHz, a decrease in the gain value of the patch array antenna and a change in the radiation angle in a direction other than the vertical direction were observed. In the case of 29 GHz, it was found that the gain value was similar to that at 28 GHz. The radiation angle was maintained in the vertical direction. In Figs. 14c and 14d, the radiation performance satisfied the CP characteristic with an AR value of less than 3 dB in

the $\theta = \pm 10^\circ$ range not only at 28 GHz but also at 29 GHz, indicating that stable CP communications may be possible in this frequency range. These measurement results suggest that this 3D printed antenna array may satisfy space antenna criteria by improving the current structure. The AR value is less than 1.5 dB in only some regions but not in the entire $\theta = \pm 10^\circ$ range.

In addition to measuring the radiation pattern, we measured whether there is an omnidirectional radiation pattern that is symmetrical and oriented vertically for azimuths of the antenna other than $\phi = 0^\circ$ and $\phi = 90^\circ$. Fig. 15a shows a 5G measurement chamber (C&G Microwave, Korea) connected to the network analyzer (Keysight PNA N5227B5G, USA), which can simultaneously measure radiation patterns in 3D through the sensors arranged therein. Fig. 15b shows the results of measuring the radiation pattern of the patch antenna array using this equipment. The fabricated patch antenna array had an ARBW value of 3.10 GHz, which is wider than 1.55 GHz of the PCB-fabricated antenna [29]. These results indicate that the fabricated patch antenna array has a CP radiation performance compared to the PCB patch antenna fabricated by a conventional method.

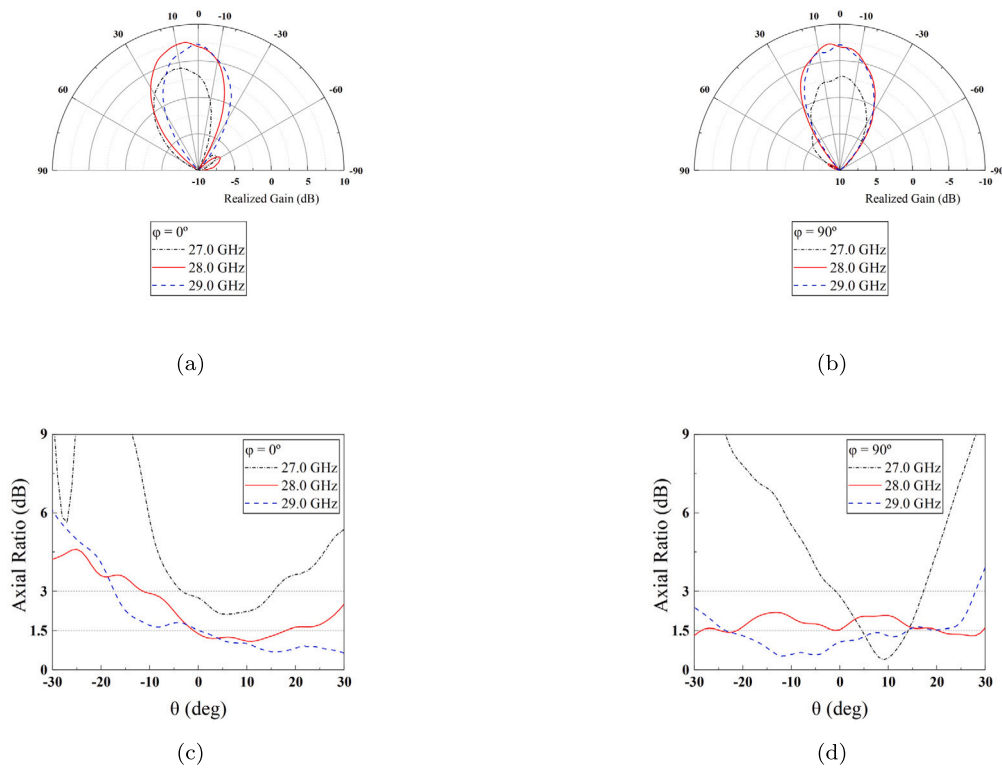


Fig. 14. Measured gain radiation patterns (a) in the $\phi = 0^\circ$, and (b) in the $\phi = 90^\circ$ and axial ratio radiation patterns (c) in the $\phi = 0^\circ$, and (d) in the $\phi = 90^\circ$ of patch antenna array for 27.0, 28.0, and 29.0 GHz.

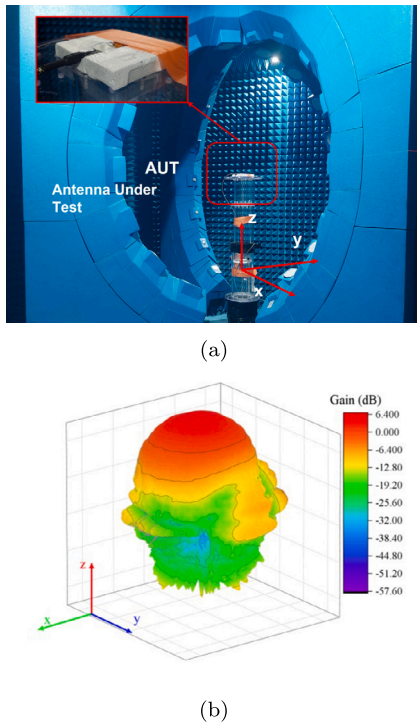


Fig. 15. (a) Far-field gain measurement in a fully 5G anechoic chamber with experimental setup system and (b) the 3D far field gain pattern of the patch antenna array at 28 GHz.

4. Conclusion

This study demonstrates the feasibility of using 3D printing technology to fabricate a compact 2×2 circularly polarized patch antenna

array for small satellite communication at 28 GHz. The proposed antenna shows promising performance in gain and circular polarization characteristics with the array displacement method and via fence structure with a separated sequentially rotated feed network, addressing the limitations of traditional PCB fabrication. Simulation results show that the arrayed antenna achieves an impedance bandwidth of 6.20 GHz, the axial ratio bandwidth of 3.49 GHz, and a 28 GHz gain of 9.31 dB. Measurement results demonstrate that the arrayed antenna achieves an impedance bandwidth of 8.00 GHz, an axial ratio bandwidth of 3.1 GHz, and a 28 GHz gain of 6.44 dB, which is well matched to the prediction of the array structure tendency from simulation results, which indicate that array displacement increases antenna performance. These performance metrics represent improvements over conventional patch antennas, enhancing the reliability of high-frequency communication in terms of compactness and circularly polarized antenna efficiency. Additionally, thermal cycling tests confirmed the antenna's durability in space environments, demonstrating its potential for space and small satellite applications.

CRedit authorship contribution statement

Jengsu Yoo: Writing – review & editing, Writing – original draft, Visualization, Validation, Methodology, Investigation, Formal analysis, Data curation, Conceptualization. **Myung Lae Lee:** Writing – review & editing, Validation, Methodology, Formal analysis, Conceptualization. **Yong Suk Yang:** Writing – review & editing, Validation, Supervision, Project administration, Formal analysis.

Declaration of competing interest

The authors declare the following financial interests/personal relationships which may be considered as potential competing interests: Yong Suk Yang reports financial support was provided by the Institute of Civil-Military Technology Cooperation (ICMTC) (22-CM-EC-23). Yong Suk Yang reports statistical analysis was provided by National Radio

Research Agency. If there are other authors, they declare that they have no known competing financial interests or personal relationships that could have appeared to influence the work reported in this paper.

Acknowledgements

This work was supported by the Institute of Civil-Military Technology Cooperation (ICMTC) program (22-CM-EC-23) funded by the Defense Acquisition Program Administration, Korea. And the authors would like to thank the National Radio Research Agency for their invaluable support and cooperation in the measurement equipment and facilities of the 5G Antenna Measurement System used in this study. The assistance provided by the Communications Conformity Assessment Center at the National Radio Research Agency was instrumental in completing the measurement and analysis processes.

Data availability

Data will be made available on request.

References

- [1] E. Claight, Global small satellite market share, size, trends, analysis, growth, forecast: by type: minisatellite, microsatellite, nanosatellite, others; by application: Earth observation and remote sensing, satellite communication, science and exploration, mapping and navigation, others; by end use; regional analysis; competitive landscape; 2024-2032, <https://www.expertmarketresearch.com/reports/small-satellite-market>, 2024. (Accessed 1 July 2024).
- [2] M. Swartwout, The first one hundred cubesats: a statistical look, *J. Small Satell.* 2 (2013) 213–233.
- [3] S. Gao, Q. Luo, F. Zhu, *Circularly Polarized Antennas*, Wiley, 2014.
- [4] X. Lin, B.C. Seet, F. Joseph, E. Li, Flexible fractal electromagnetic bandgap for millimeter-wave wearable antennas, *IEEE Antennas Wirel. Propag. Lett.* 17 (2018) 1281–1285, <https://doi.org/10.1109/LAWP.2018.2842109>.
- [5] M.C. Tang, T. Shi, R.W. Ziolkowski, A study of 28 ghz, planar, multilayered, electrically small, broadside radiating, Huygens source antennas, *IEEE Trans. Antennas Propag.* 65 (2017) 6345–6354, <https://doi.org/10.1109/TAP.2017.2700888>.
- [6] X. Bai, S.-W. Qu, R.-L. Xia, Ka-band cavity-backed detached crossed dipoles for circular polarization, *IEEE Trans. Antennas Propag.* 62 (2014) 5944–5950, <https://doi.org/10.1109/TAP.2014.2358688>.
- [7] H.H. Tran, K. Nguyen-Dang, N. Hussain, Single-layer wideband circularly polarized antenna using non-uniform metasurface for c-band applications, *Comput. Mater. Continua* 68 (2021) 2487–2498, <https://doi.org/10.32604/cmc.2021.016027>.
- [8] S.X. Ta, I. Park, Low-profile broadband circularly polarized patch antenna using metasurface, *IEEE Trans. Antennas Propag.* 63 (2015) 5929–5934, <https://doi.org/10.1109/TAP.2015.2487993>.
- [9] N. Hussain, M.-J. Jeong, A. Abbas, T.-J. Kim, N. Kim, A metasurface-based low-profile wideband circularly polarized patch antenna for 5g millimeter-wave systems, *IEEE Access* 8 (2020) 22127–22135, <https://doi.org/10.1109/ACCESS.2020.2969964>.
- [10] C. Hilary, S. Nkimbeng, H. Wang, I. Park, Coplanar waveguide-fed bidirectional same-sense circularly polarized metasurface-based antenna, *J. Electromagn. Eng. Sci.* 21 (2021) 210–217, <https://doi.org/10.26866/jees.2021.3.r.28>.
- [11] C.A. Balanis, *Antenna Theory: Analysis and Design*, 4th edition, John Wiley & Sons, 2016.
- [12] J. Mass, E. Vassy, Doppler effect of artificial satellites, *Adv. Space Sci. Technol.* 4 (1962) 1–38, <https://doi.org/10.1016/B978-1-4831-9962-7.50006-2>.
- [13] F. Hibberd, The effect of the ionosphere on the Doppler shift of radio signals from an artificial satellite, *J. Atmos. Terr. Phys.* 12 (1958) 338–340, [https://doi.org/10.1016/0021-9169\(58\)90065-5](https://doi.org/10.1016/0021-9169(58)90065-5).
- [14] Z. Gal, D. Talbi, Insights into low Earth orbit satellite communication dynamics: quality of service analysis of connection behavior, latency, and Doppler shift, in: 2024 IEEE 4th International Conference on Electronic Communications, Internet of Things and Big Data (ICEIB), IEEE, 2024, pp. 116–121.
- [15] B.-H. Yeh, J.-M. Wu, R.Y. Chang, Efficient Doppler compensation for Leo satellite downlink ofdma systems, *IEEE Trans. Veh. Technol.* (2024) 1–15, <https://doi.org/10.1109/TVT.2024.3437430>.
- [16] M. Elahi, S. Trinh-Van, Y. Yang, K.-Y. Lee, K.-C. Hwang, Compact and high gain 4×4 circularly polarized microstrip patch antenna array for next generation small satellite, *Appl. Sci.* 11 (2021) 8869, <https://doi.org/10.3390/app11198869>.
- [17] H. Baghdadi, G. Royo, I. Bel, F.J. Cortés, S. Celma, Compact 2×2 circularly polarized aperture-coupled antenna array for ka-band satcom-on-the-move applications, *Electronics* 10 (2021), <https://doi.org/10.3390/electronics10141621>.
- [18] K. Trzebiatowski, W. Kalista, M. Rzymowski, L. Kulas, K. Nyka, Multibeam antenna for ka-band cubesat connectivity using 3-d printed lens and antenna array, *IEEE Antennas Wirel. Propag. Lett.* 21 (2022) 2244–2248, <https://doi.org/10.1109/LAWP.2022.3189073>.
- [19] MIL-STD-188-164A, *Interoperability of SHF Satellite Communications Terminals*, The United States Department of Defense, 2009.
- [20] W.-H. Lim, S.-M. Moon, H.L. Lee, Ka-band flat panel circularly polarized antenna array for Leo satellite communication systems, *Alex. Eng. J.* 78 (2023) 584–591, <https://doi.org/10.1016/j.aej.2023.07.081>.
- [21] J. Wei, S. Liao, Q. Xue, W. Che, Wideband circularly polarized phased array antenna for k/ka-band satellite communication using me-dipole elements, *IEEE Antennas Wirel. Propag. Lett.* (2024), <https://doi.org/10.1109/LAWP.2024.3398056>.
- [22] A. Chrysler, C. Furse, R.N. Simons, F.A. Miranda, A ka-band (26 ghz) circularly polarized 2×2 microstrip patch sub-array with compact feed, in: 2017 IEEE International Symposium on Antennas and Propagation & USNC/URSI National Radio Science Meeting, IEEE, 2017, pp. 1447–1448.
- [23] J. Huang, A ka-band circularly polarized high-gain microstrip array antenna, *IEEE Trans. Antennas Propag.* 43 (1995) 113–116, <https://doi.org/10.1109/8.366361>.
- [24] P. Hall, C. Hall, Coplanar corporate feed effects in microstrip patch array design, *IEE Proc., H Microw. Antennas Propag.* 135 (1988) 180, <https://doi.org/10.1049/ip-h-2.1988.0038>.
- [25] N. Supreeyattitkul, D. Torrungrueng, C. Phongcharoenpanich, Quadri-cluster broadband circularly-polarized sequentially-rotated metasurface-based antenna array for c-band satellite communications, *IEEE Access* 9 (2021) 67015–67027, <https://doi.org/10.1109/ACCESS.2021.3075994>.
- [26] A. Chen, Y. Zhang, Z. Chen, C. Yang, Development of a ka-band wideband circularly polarized 64-element microstrip antenna array with double application of the sequential rotation feeding technique, *IEEE Antennas Wirel. Propag. Lett.* 10 (2011) 1270–1273, <https://doi.org/10.1109/LAWP.2011.2175433>.
- [27] P. Hall, J. Dahele, J. James, Design principles of sequentially fed, wide bandwidth, circularly polarised microstrip antennas, *IEE Proc., H Microw. Antennas Propag.* 136 (1989) 381, <https://doi.org/10.1049/ip-h-2.1989.0069>.
- [28] M. Sun, N. Liu, L. Zhu, G. Fu, Wideband circularly polarized sequentially rotated microstrip antenna array with sequential-phase feeding network, *J. Commun. Inf. Netw.* 5 (2020) 350–357, <https://doi.org/10.23919/JCIN.2020.9200898>.
- [29] A. Chen, Y. Zhang, Z. Chen, S. Cao, A ka-band high-gain circularly polarized microstrip antenna array, *IEEE Antennas Wirel. Propag. Lett.* 9 (2010) 1115–1118, <https://doi.org/10.1109/LAWP.2010.2093866>.
- [30] A. Piroutiniya, M.H. Rasekhanmeh, P. Mohammadi, Wide-band circularly polarised antenna array using sequential phase feed structure and reinforced square radiating patch element, *IET Microw. Antennas Propag.* 12 (2018) 1395–1399, <https://doi.org/10.1049/iet-map.2017.1075>.
- [31] A. Chen, C. Yang, Z. Chen, Y. Zhang, Y. He, Design of multilevel sequential rotation feeding networks used for circularly polarized microstrip antenna arrays, *Int. J. Antennas Propag.* (2012) 2012, <https://doi.org/10.1155/2012/304816>.
- [32] Y. Zou, H. Li, Y. Xue, B. Sun, A high-gain compact circularly polarized microstrip array antenna with simplified feed network, *Int. J. RF Microw. Comput.-Aided Eng.* 29 (2019), <https://doi.org/10.1002/mcme.21964>.
- [33] F. Karami, P. Rezaei, A.A.e Elahi, M. Sharifi, J.S. Meiguni, Efficient transition hybrid two-layer feed network: polarization diversity in a satellite transceiver array antenna, *IEEE Antennas Propag. Mag.* 63 (2021) 51–60, <https://doi.org/10.1109/MAP.2019.2943314>.
- [34] J. Zeng, K.M. Luk, Single-layered broadband magnetoelectric dipole antenna for new 5g application, *IEEE Antennas Wirel. Propag. Lett.* 18 (2019) 911–915, <https://doi.org/10.1109/LAWP.2019.2905768>.
- [35] R.V. Gatti, R. Rossi, M. Dionigi, Single-layer line-fed broadband microstrip patch antenna on thin substrates, *Electronics* 10 (2020) 1–14, <https://doi.org/10.3390/electronics10010037>.
- [36] M.I. Nawaz, Z. Huiling, M.S.S. Nawaz, K. Zakim, S. Zamin, A. Khan, A review on wideband microstrip patch antenna design techniques, in: 2013 International Conference on Aerospace Science & Engineering (ICASE), IEEE, 2013, pp. 1–8.
- [37] A.A. Samat, D.N.K.A. Zaidel, D.A.A. Mat, M.R.M. Sharip, D.N.A. Zaidel, I.I. Muhamad, Y.L. Then, Surface current distribution and performance analysis of different feeding techniques for microstrip patch antenna, in: 2020 13th International UNIMAS Engineering Conference (EnCon), IEEE, 2020, pp. 1–5.
- [38] Y. Wang, X. Zhang, R. Su, M. Chen, C. Shen, H. Xu, R. He, 3d printed antennas for 5g communication: current progress and future challenges, *Chin. J. Mech. Eng. Addit. Manuf. Front.* 2 (2023) 100065, <https://doi.org/10.1016/j.cjmeam.2023.100065>.
- [39] S.S. Carvalho, J.R. Reis, A. Mateus, R.F. Caldeirinha, Exploring design approaches for 3d printed antennas, *IEEE Access* 12 (2024) 10718–10735, <https://doi.org/10.1109/ACCESS.2024.3354372>.
- [40] L. Liu, Y. Yang, S. Li, X. Fang, F. Meng, C. Yu, A 3d printed ka-band high-efficiency wide-slit antenna array for high-power microwave applications, *Int. J. Antennas Propag.* 2022 (2022) 1–8, <https://doi.org/10.1155/2022/2653410>.
- [41] B. Zhang, Y.-X. Guo, H. Sun, Y. Wu, Metallic, 3d-printed, k-band-stepped, double-ridged square horn antennas, *Appl. Sci.* 8 (2017) 33, <https://doi.org/10.3390/app8010033>.
- [42] J.J. Adams, E.B. Duoss, T.F. Malkowski, M.J. Motala, B.Y. Ahn, R.G. Nuzzo, J.T. Bernhard, J.A. Lewis, Conformal printing of electrically small antennas on three-dimensional surfaces, *Adv. Mater.* 23 (2011) 1335–1340, <https://doi.org/10.1002/adma.201003734>.
- [43] A.C. Paoletta, D. Silva-Saez, D. Kozlovski, R. Even, 3-d printed rf amplifier for wireless systems, in: 2019 IEEE Radio and Wireless Symposium (RWS), IEEE, 2019, pp. 1–3.

- [44] I. Marasco, G. Niro, F. Rizzi, A. D'Orazio, M.D. Vittorio, M. Grande, Dual band flexible planar inverted-f antenna for internet of healthcare things applications, in: *Mediterranean Microwave Symposium*, vol. 2022-May, IEEE Computer Society, 2022, pp. 1–4.
- [45] R. Bahr, B. Teharani, M.M. Tentzeris, K. Byers, A novel integration of stereolithography and inkjet printing for multichip modules with high frequency packaging applications, in: *Proceedings - Electronic Components and Technology Conference*, vol. 2018-May, Institute of Electrical and Electronics Engineers Inc., 2018, pp. 2498–2504.
- [46] M. Li, Y. Yang, F. Jacopi, M. Yamada, J. Nulman, Compact multilayer bandpass filter using low-temperature additively manufacturing solution, *IEEE Trans. Electron Devices* 68 (2021) 3163–3169, <https://doi.org/10.1109/TED.2021.3072926>.
- [47] I. Marasco, G. Niro, L. Lamanna, L. Piro, F. Guido, L. Algieri, V. Mastronardi, A. Qualtieri, E. Scarpa, D. Desmaële, F. Rizzi, A. D'Orazio, M.D. Vittorio, M. Grande, Compact and flexible meander antenna for surface acoustic wave sensors, *Microelectron. Eng.* 227 (2020) 111322, <https://doi.org/10.1016/j.mee.2020.111322>.
- [48] S. Fried, 3d printing technologies for electronics, *J. Imag. Soc. Jpn.* 56 (6) (2017) 617–620, <https://doi.org/10.11370/isj.56.617>.
- [49] M. Safarabadi, S. Bazargan, Prediction of equivalent static loads act on a micro satellite via modal analysis, *Eng. Solid Mech.* 3 (2) (2015) 75–84, <https://doi.org/10.5267/j.esm.2015.2.004>.
- [50] M. Safarabadi, J. Haghshenas, H. Izi, H. Koochaki Kellardeh, Design of micro-vibration isolation system for a remote-sensing satellite payload using viscoelastic materials, *Eng. Solid Mech.* 8 (1) (2020) 69–76, <https://doi.org/10.5267/j.esm.2019.8.003>.
- [51] H. Emami, F. Farhani, M. Safarabadi, Influence of modal effective mass distribution on the static and dynamic behavior of a satellite structure under base excitations, *Mater. Sci. Res. India* 5 (2) (2008) 209–218, <https://doi.org/10.13005/msri/50201>.
- [52] M. Mobarakian, M. Safarabadi, M. Farahani, Investigating the effects of cooling rate on distortion of asymmetric composite laminates, *Compos. Struct.* 236 (2020) 111875, <https://doi.org/10.1016/j.compstruct.2020.111875>.
- [53] M. Mobarakian, M. Safarabadi, M. Farahani, Developing a thermomechanical and thermochemical model for investigating the cooling rate effects on the distortion of unsymmetrical viscoelastic polymeric composite laminates, *Polym. Test.* 87 (April 2020) 106503, <https://doi.org/10.1016/j.polymertesting.2020.106503>.
- [54] M. Zahed, R. Ardeshiri Jouneghani, M. Safarabadi, Reinforcement of 3d-printed re-entrant structures using additional supports under three-point bending, experimental and numerical analyses, *Adv. Eng. Mater.* 26 (1) (Jan. 2024), <https://doi.org/10.1002/adem.202301252>.
- [55] NanoDimension, Dragonfly ldm lightsout digital manufacturing system, <https://www.nano-di.com/ame-dragonfly-ldm>, 2023. (Accessed 20 March 2024).
- [56] M.P. David, *Microwave Engineering*, 4th edition, John Wiley & Sons, 2011.
- [57] P.-S. Kildal, *Foundations of Antenna Engineering: A Unified Approach for Line-of-Sight and Multipath*, Artech, 2015.
- [58] L. Fernandez, J.F. Munoz-Martin, J.A.R. de Azua, A. Calveras, A. Camps, Design and validation of a dual-band circular polarization patch antenna and stripline combiner for the fssc mission, *Acta Astronaut.* 208 (2023) 194–204, <https://doi.org/10.1016/j.actaastro.2023.03.042>.
- [59] T. Mitha, M. Pour, Principles of adaptive element spacing in linear array antennas, *Sci. Rep.* 11 (2021), <https://doi.org/10.1038/s41598-021-84874-7>.
- [60] R.P. Tortorich, W. Morell, E. Reiner, W. Bouillon, J.-W. Choi, A study on the radiated susceptibility of printed circuit boards and the effects of via fencing, *Electronics* 10 (2021) 539, <https://doi.org/10.3390/electronics10050539>.
- [61] G. Ponchak, D. Chun, J.-G. Yook, L. Katehi, The use of metal filled via holes for improving isolation in ltcc rf and wireless multichip packages, *IEEE Trans. Adv. Packaging* 23 (2000) 88–99, <https://doi.org/10.1109/6040.826766>.
- [62] Z. Qi, X. Li, J. Chu, J. Xiao, H. Zhu, High-gain cavity backed patch antenna arrays at 140 ghz based on ltcc technology, *Int. J. Microw. Wirel. Technol.* 11 (2019) 829–834, <https://doi.org/10.1017/S175907871900031X>.
- [63] J. Li, S. Yan, R. Cai, Thermal analysis of composite solar array subjected to space heat flux, *Aerosp. Sci. Technol.* 27 (2013) 84–94, <https://doi.org/10.1016/j.ast.2012.06.010>.
- [64] ECSS-Q-ST-70-02C, *Space Product Assurance - Thermal Vacuum Outgassing Test for the Screening of Space Materials*, European Space Agency, 2008.
- [65] ECSS-Q-ST-70-10C, *Space Product Assurance - Qualification of Printed Circuit Boards*, European Space Agency, 2008.